

# An all-optical, in situ diagnostic for large molecule and nanoparticle detection

Alexandros Gerakis<sup>a</sup>, Mikhail N. Shneider<sup>b</sup>, Brentley C. Stratton<sup>a</sup> and Yevgeny Raitses<sup>a</sup>

<sup>a</sup>Princeton Plasma Physics Laboratory, 100 Stellarator Road, Princeton, NJ, 08540, USA

<sup>b</sup>Department of Mechanical and Aerospace Engineering, Princeton University, Princeton, NJ 08544, USA

## ABSTRACT

We report on the development and application of a new laser diagnostic for the in situ detection of large molecules and nanoparticles. This four wave mixing diagnostic technique relies on the creation of an optical lattice in a medium due to the interaction between polarized particles and intense laser fields. Though this interaction, we can detect the temperature, pressure, relative density, polarizability and speed of sound of a gas and gas mixture. This diagnostic was already successfully demonstrated in atomic and molecular gaseous environments, where the different gas polarizabilities and pressures were successfully measured. We are currently conducting measurements with large molecules and nanoparticles, the results of which will be presented in this meeting.

**Keywords:** Rayleigh, Brillouin, scattering, spectroscopy, optical lattices

## 1. INTRODUCTION

Coherent Rayleigh-Brillouin Scattering (CRBS) is a non-resonant, four wave mixing technique which, since it was initially demonstrated,<sup>1,2</sup> has been employed as a useful tool for the determination of the temperature, speed of sound, shear and bulk viscosity of a gas or gas mixture.<sup>3–8</sup> Recently it was also demonstrated how CRBS can be used for the measurement of the polarizability of a gas or gas mixture.<sup>9</sup> CRBS offers the important advantage that the scattered signal is a coherent laser beam, in comparison to spontaneous Rayleigh-Brillouin scattering (SRBS) in which the signal is scattered in a  $4\pi$  solid angle. In comparison to SRBS then, CRBS allows for measurements at a long distance, without any sacrifice in the signal to noise ratio (SNR) as is the case with SRBS in which the signal detector has to ideally be placed as close as possible to the measurement region. Additionally, due its four-wave mixing nature it offers a high degree of spatial localization (typically  $150 - 200\mu\text{m}$ ) in comparison to SRBS which is a more line of sight technique. Finally, although in SRBS the signal intensity  $I_s$  is proportional to the number of scatterers  $N$ , the CRBS signal intensity  $I_s$  is proportional to  $N^2$ .<sup>9,10</sup>

In CRBS two beams of wavelength  $\lambda_{pump}$  (called the *pumps*) with a set frequency difference  $\Delta\omega$  cross at an angle  $\phi$  within a medium to create an optical lattice, due to electrostriction. The resultant optical lattice has got a wavelength  $\lambda_g = \lambda_{pump}/(2 \sin \phi)$  and a phase velocity  $v$  given by  $v = (\omega_1 - \omega_2)/(\mathbf{k}_1 - \mathbf{k}_2) = (\Delta\omega \cdot \lambda_{pump})/(2 \cdot \sin \phi)$ , where  $\phi$  is the half angle between the two pump beams (Fig. 1). A third beam (called the *probe*) of wavelength  $\lambda_{probe}$  is incident upon this lattice at the Bragg angle  $\theta = \sin^{-1}(\lambda_{probe}/(2 \cdot \lambda_g))$ . The interaction of the probe with the optical lattice generates the formation of a fourth coherent beam, called the *signal*. The CRBS spectrum is the record of the intensity of the signal beam with respect to  $\Delta\omega$  and it consists of three distinct peaks. One is the Rayleigh peak, centered around  $\Delta\omega = 0$ , which is Doppler broadened due to the thermal motion of the medium. Equally shifted around it and centered at the speed of sound are the two Brillouin peaks due to acoustic (pressure) waves launched in the medium. Typical acquisition times for a CRBS spectrum are usually within 5 – 20 minutes, unless a chirped lattice approach is used through which a CRBS spectrum can be acquired within a single laser pulse of  $\sim 150\text{ns}$  duration directly on the oscilloscope screen, without the need for data post-processing.<sup>11</sup>

Further author information: (Send correspondence to A. Gerakis)  
E-mail: agerakis@pppl.gov, Telephone: 1 609 243 3903

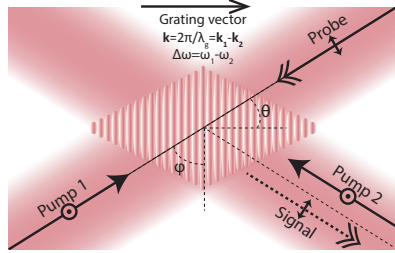


Figure 1. Schematic of a typical CRBS geometry. Two almost counter-propagating, equipolarized pump beams cross within a medium at a half-angle  $\phi$  to create an optical lattice. A probe beam, normally polarized to the pumps, is incident at this lattice at the Bragg angle  $\theta$  and is being scattered from it producing a signal beam, which maintains all the spatial and polarization characteristics of the probe beam.

In this paper we present a laser system designed and developed at the Princeton Plasma Physics Laboratory (PPPL) which utilizes the chirped lattice approach. We will present the operation of the laser system as a whole as well as its constituent subsystems and how we have used it for the determination of the relative polarisability of a gas or gas mixture. Finally, we will show how we aim to use this setup for the measurement of nanoparticles produced in a graphitic arc discharge.

## 2. THE LASER SYSTEM

A general schematic of the laser system used for single shot CRBS can be seen in Fig. 2. The system can be divided in two main sections: beam preparation and pulse amplification. In the beam preparation, two low energy laser pulses with a chirped frequency difference  $\Delta\omega$  are being created. In order to reach the high intensities needed for CRBS (in the order of  $\sim 150 - 200$  mJ per pulse per beam) these pulses are being further amplified through two custom made, triple-stage, diode pumped amplifiers. In the next sections, we describe the operation of each of the subsystems used in the CRBS laser system.

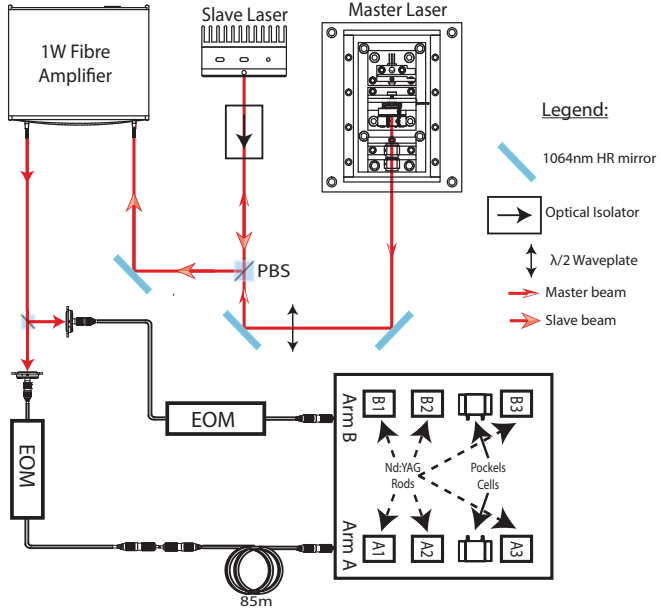


Figure 2. Schematic of the laser system for single shot CRBS developed at PPPL. The chirped continuous wave (CW) laser beam is initially produced at the master laser which is injection locked to a slave laser, emitting at the same laser frequency. This beam is further amplified by a commercial fiber amplifier. The resulting beam is being "chopped" into pulses by two electro-optic intensity modulators before being fed to the two arms of a custom made pulsed amplifier.

## 2.1 The master laser

The master laser is custom, in-house made and is essentially the element in the laser system responsible for creating the laser pulses with a chirped laser frequency. A rendering of the master laser can be seen in Fig. 3. As can be seen, the pump diode and the actual laser cavity and being thermally controlled by two different Peltier elements but they both dissipate the produced thermal load on the same copper block. The Nd:YVO<sub>4</sub> laser crystal which is the active lasing medium is being pumped by a commercial laser diode which emits at 808 nm (Thorlabs L808P1000MM). The Nd:YVO<sub>4</sub> laser crystal measures 3x3x0.5 mm and is anti-reflection (AR) coated on one side for 808 nm and high-reflection (HR) coated for 1064 nm on the other side. The laser cavity is then formed by the laser crystal on one side and by a 100 mm, 97.5% partially-reflection (PR) coated for 1064 nm output coupler on the other side, while the total cavity length measures  $\sim 5$  mm. In comparison to a similar laser presented in Ref.<sup>12</sup> where a plano-parallel configuration was used and was totally relying on thermal lensing on the crystal to achieve lasing, we opted for a plano-concave configuration since this way we fall within the operational boundaries as posed by the cavity stability criterion, as shown on Fig. 4. The cavity stability criterion is expressed as  $0 \leq g_1 g_2 \leq 1$ , where  $g_1 = 1 - \frac{L}{R_1}$  and  $g_2 = 1 - \frac{L}{R_2}$ , where  $L$  is the cavity length and  $R_1$ ,  $R_2$  the radii of curvature of the two surfaces forming the cavity.

The optical component that allows for the chirping of the laser output is an intracavity LiTaO<sub>3</sub> electro-optic modulator (EOM) crystal, which is AR coated for 1064 nm on both sides and is gold plated on the top and bottom while it measures at 1x3x5 mm. By applying voltage to the EOM, the laser cavity length changes because of a change in the refractive index of the crystal, resulting in a change in the laser frequency. The voltage to the EOM is supplied via a waveform generator (Hewlett-Packard 3314A) the output of which is further amplified by commercial voltage amplifier (A.A. Lab Systems A303). It is important for as much as possible of the cavity length to be comprised by the EOM. The frequency change  $\delta f$  of the laser output, with respect to the applied voltage  $\delta V$  to the electrodes of the LiTaO<sub>3</sub> crystal, is given by:<sup>13</sup>

$$\delta f = \frac{\eta \cdot n_1^2 \cdot r_{33} \cdot f_{opt}}{2 \cdot d} \frac{n_1 \cdot l_1}{n_1 \cdot l_1 + n_2 \cdot l_2 + n_3 \cdot l_3} \delta V \quad (1)$$

where  $l_1$ ,  $l_2$  and  $l_3$  are the lengths of the LiTaO<sub>3</sub> crystal, the Nd:YVO<sub>4</sub> crystal and the air gap, respectively, while  $n_1$ ,  $n_2$  and  $n_3$  their respective refractive indeces. The coupling efficiency between the electric field and the

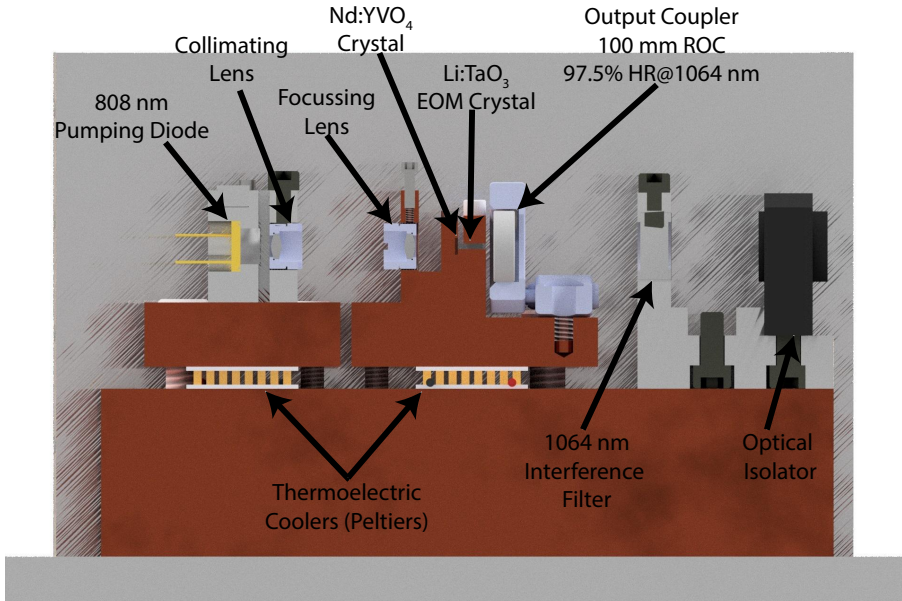


Figure 3. Rendering of the master laser used in the laser system presented in this paper. Seen from the left to right are the pumping block, housing the 808 nm pump diode, the cavity block, housing the Nd:YVO<sub>4</sub> laser crystal, the LiTaO<sub>3</sub> EOM and the output coupler and the filter block, housing the 1064 nm interference filter and the optical isolator.

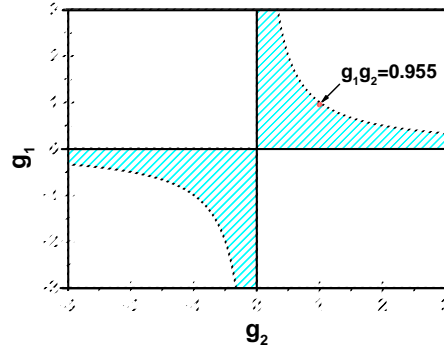


Figure 4. Laser stability diagram showing the  $g_1g_2$  value for the laser cavity used in the master laser. The chosen plano-concave configuration allows the cavity to fall within the boundaries set by the stability criterion. A plano-parallel configuration would have resulted a  $g_1g_2$  value of 1, making such a cavity dependant on thermal lasing on the crystal in order to lase.

laser cavity mode is given by  $\eta$ ,  $d$  is the thickness of the LiTaO<sub>3</sub> crystal and  $r_{33}$  its electro-optic coefficient. It is apparent from Eq. 1 that the smaller the product  $n_3 \cdot l_3$ , the larger the chirping rate the laser can achieve. Besides, the shorter the laser cavity, the larger the free spectral range (FSR) and thus the larger the resulting mode hop free tuning range. The FSR is given by:<sup>14</sup>

$$\Delta f_{ax} = \frac{c_0}{2 \cdot n \cdot L} \quad (2)$$

where  $n$  is the refractive index inside the cavity and  $L$  is the cavity's length. It is noteworthy that although ideally the air gap should be zero, in practice some distance between the crystals is desired in order to eliminate the possibility of one of the crystals breaking due to mechanical pressure.

Fig. 5 presents the optical efficiency curves for this laser, both with and without the intracavity EOM. Without the intracavity EOM an optical-to-optical efficiency of  $\sim 26.5\%$  is achieved, while with the intracavity EOM in place, this efficiency drops to  $\sim 20.5\%$ , as expected due to the additional loss mechanism within the cavity. The efficiencies both with and without the EOM are satisfactory for such a type of laser, allowing for output powers in excess of 200 mW in both cases.

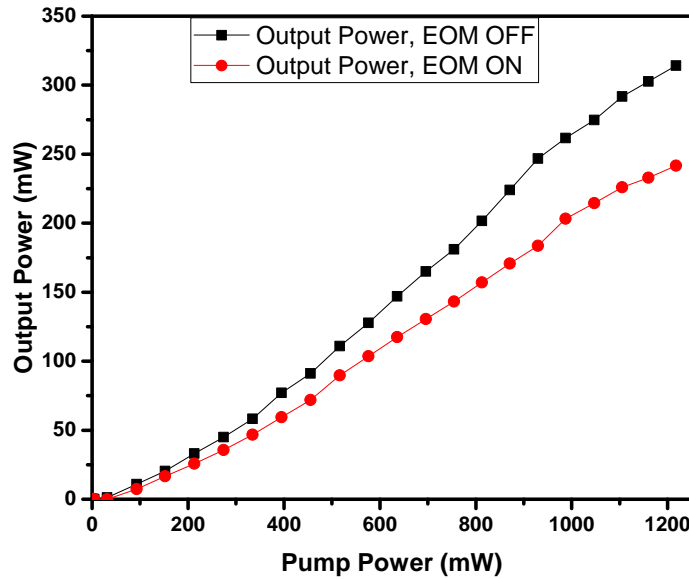


Figure 5. Optical-to-optical conversion efficiencies for the master laser with and without the intracavity EOM.

## 2.2 The slave laser

The output of the Nd:YVO<sub>4</sub> master laser is coupled into a second laser diode emitting at  $\sim 1064$  nm in a master-slave configuration. The reason behind using this configuration is so that we can discard the relaxation oscillations that are occurring on the master laser. The term "relaxation oscillations" is used in order to describe the "small-amplitude, quasi-sinusoidal, exponentially damped oscillations about the steady-state amplitude which occur when a continuously operated laser is slightly disturbed".<sup>14</sup> In other words, any change in the operating conditions of a solid-state laser like the one we are using, such as a slight change in the cavity length due to voltage being applied to the EOM, will induce intensity oscillations at the output. These intensity oscillations occur in laser systems in which the upper state lifetime is substantially longer than the laser cavity decay time, which is defined as  $\tau_c = T/\delta_c$ , where  $T = 2L/c$  is the cavity roundtrip time and  $\delta_c$  are the round-trip losses.

Relaxation oscillations can be described quite accurately through two coupled non-linear differential equations, often termed the Statz-DeMars equations:

$$\overbrace{\frac{dN}{dt}}^1 = \underbrace{\Lambda}_2 - \underbrace{\frac{N}{\tau_2}}_3 - \underbrace{I \cdot N \cdot \frac{\sigma}{h \cdot \nu}}_4 \quad (3a)$$

$$\underbrace{\frac{dI}{dt}}_5 = \underbrace{c \cdot \sigma \cdot N \cdot I \cdot \frac{l}{L}}_6 - \underbrace{\frac{I}{\tau_{cav}}}_7 \quad (3b)$$

where  $N$  is the upper-state population,  $\Lambda$  is the upper-state excitation rate,  $\tau_2$  is the upper-state lifetime,  $I$  is the laser intensity,  $\sigma$  is the stimulated emission cross-section,  $l$  is the length of the active medium,  $L$  the length of the cavity and  $\tau_{cav} = \frac{2L}{\beta c}$  the cavity decay lifetime parameter, where  $\beta$  are the scattering losses within the cavity. The numbered terms in equations 3 denote:

1. The rate of increase of the upper-state population per unit time.
2. The excitation rate to the upper-state.
3. The decay rate due to spontaneous emission.
4. Probability of photon interaction with the active medium per unit time.
5. The rate of intensity output per unit time.
6. The total gain per unit volume and,
7. The total cavity losses per round trip.

Essentially equations 3 describe the evolution of the upper-state population of the active medium coupled with the output intensity of the laser. These two terms would oscillate around the steady-state solution for some time before eventually reaching it. This happens because as the upper-state population reaches its peak, it gets very sharply depleted, resulting in a very sharp spike in the intensity profile. Once depleted (but to a higher level than the initial), it starts building up again because of the pump, while the intensity of course drops. This process keeps on repeating itself until an operational steady state is reached. Once though the laser's operating conditions change again, this process re-initiates. Figure 6 is a plot of the relaxation oscillations for the same cavity for Nd:YAG and Nd:YVO<sub>4</sub>, from zero pumping ( $t < 0$ ) to three times the threshold pumping ( $t > 0$ ), showing the dependence of relaxation oscillations on the upper state lifetime (230  $\mu$ s and 100  $\mu$ s respectively).

The faster decay of the relaxation oscillations is one of the reasons for choosing to use Nd:YVO<sub>4</sub> instead of Nd:YAG in the master laser, although the timescale over which these occur is still large compared to the duration of the pulses we wish to ultimately use. Hence, by using the aforementioned master-slave configuration we are forcing the slave diode laser to emit at the master's frequency, without it being affected by the variations in the

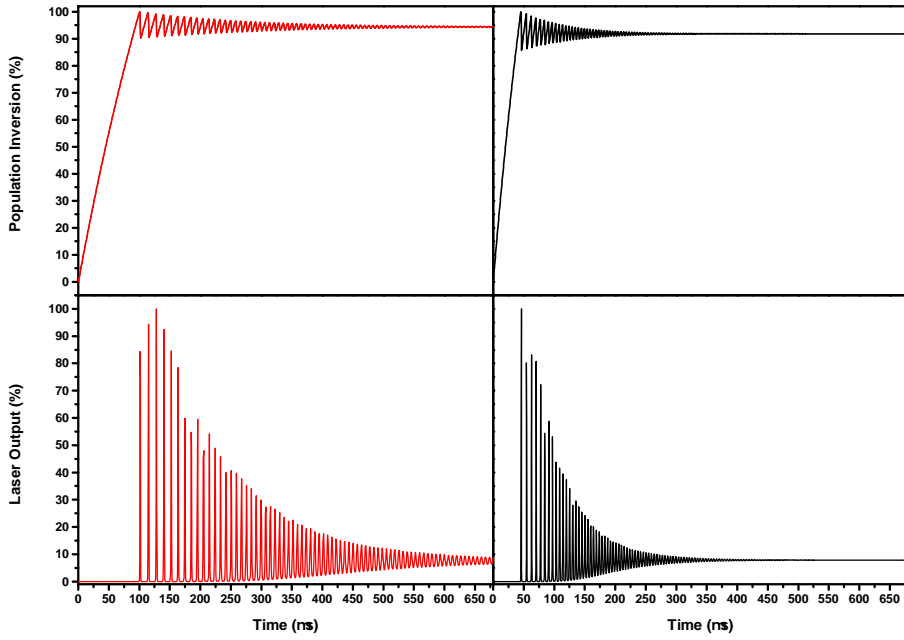


Figure 6. Relaxation oscillations for Nd:YAG (red) and Nd:YVO<sub>4</sub> (black). Due to the shorter upper state lifetime, the Nd:YVO<sub>4</sub> relaxes to the steady-state conditions faster than the Nd:YAG based cavity.

output intensity. The 1064 nm diode we use (Thorlabs M9-A64 – 0200) can thus emit up to 200 mW at the same frequency as the master laser.

In order to monitor the induced frequency chirp on the master laser, we monitor the output of the slave on a commercial scanning Fabry-Perot interferometer (Thorlabs SA200 – 8B). We drive the EOM with a continuous sinusoidal wave, and measure the induced chirp as described in Ref.<sup>12,15,16</sup> Fig. 7 shows the measured chirp with respect to the applied voltage. The resulting chirp rate was measured to be 4 MHz/V, which is lower than the one reported in other similar lasers.<sup>12,16</sup> This is attributed to the poor electrical connection between the electrodes and the LiTaO<sub>3</sub> crystal at the time of the measurement and is something that can be improved in the system.

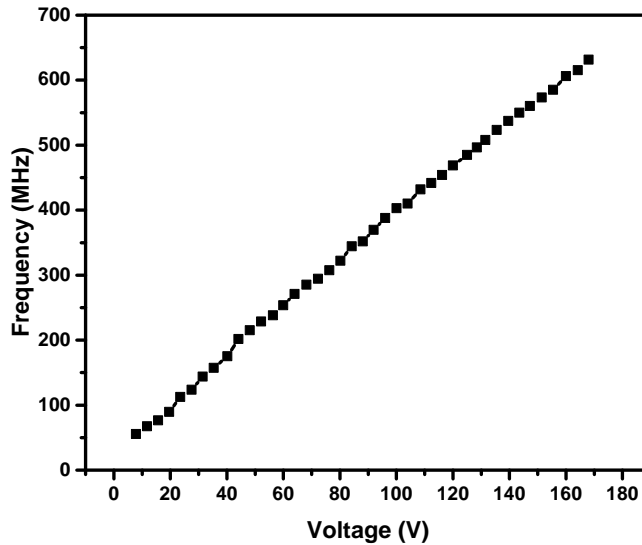


Figure 7. Measured chirp on the master laser with respect to applied voltage on the intracavity EOM.

### 2.3 Further amplification, pulse shaping and chirp

The output of the slave laser is further amplified by an Ytterbium based commercial fiber amplifier (IPG Photonics, YAR-1K-1064-LP-SF) which emits up to 1 W of optical power at the same frequency as the input beam. The output of the fiber amplifier is then split in two and the resulting beams are respectively being fed into two commercial LiTaO<sub>3</sub> intensity electro-optic modulators (IEOM, Jenoptik AM1064b). These intensity modulators are essentially Mach-Zender type interferometers which allow fast chopping of the input CW beam into optical pulses, the temporal profile of which is determined by the input voltage temporal profile. Although this type of EOMs is well known to drift within the duration of a day causing instabilities in its operation, it offers the advantage over Pockel's cell type switches (such as the one used in Ref.<sup>12</sup>) that they can be driven with low voltages in the order of 0 – 10 V which can easily be provided by a standard waveform generator instead of the fast switching in the kV range that is required to drive the Pockel's cells. The two intensity modulators described here are being driven by a commercial arbitrary waveform generator (Tektronix AFG3102C), which we are controlling with a custom written LabVIEW program which allows us to draw voltage pulses (and thus ultimately optical pulses) on the computer screen.

Fig. 8 presents the way the chirped pulses are being produced. We open the first IEOM for the first, unchirped pulse to go through and when we open the second IEOM for the second pulse, we send a voltage signal on the master's intracavity EOM to establish a frequency relation between the two pulses. In order to accommodate for the time difference between the two events, the first, unchirped pulse, travels through an optical delay line of 85 m. The main advantage of this setup in comparison to other setups where two commercial high power lasers are being referenced to one another, is that this way the produced pulses are self-referenced within a timeframe of 500 ns thus eliminating the effect of any thermal instabilities in the system.

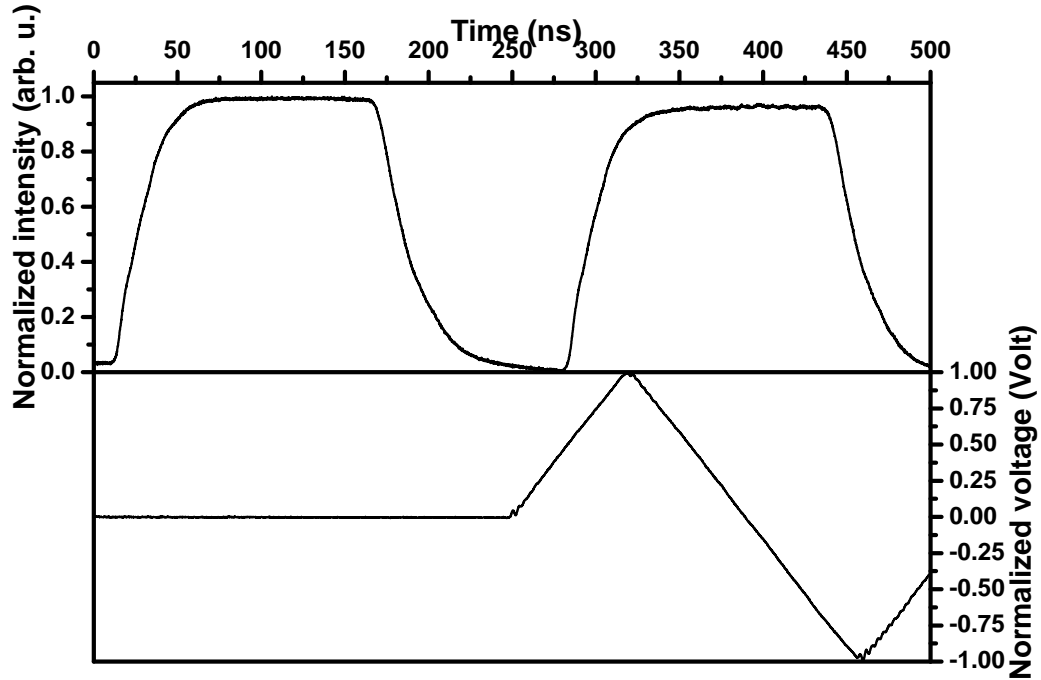


Figure 8. Schematic of the way the chirped pulses are being produced in this system. On the top plot are shown the two pulses while on the plot below the voltage applied to the master's intracavity EOM is shown. The resulting optical chirp on the pulses is ultimately dependent on the voltage waveform that we apply to the intracavity EOM.

### 2.4 Pulsed amplification

The last stage of the laser system relies in the further amplification of the produced pulses. Two identical arms providing pulsed amplification for the respective pulses have been built. These amplify the  $\sim 100$  nJ pulses produced in the pulse preparation stage to approximately  $\sim 200$  mJ in the output. They each comprise of three

diode pumped amplifiers in series (all from Northrop-Grumman Cutting Edge Optronics): an RBAT20-1P200 amplifying from  $\sim 100$  nJ to  $\sim 12 \mu\text{J}$ , an RBAT34-1P200 amplifying from  $\sim 12 \mu\text{J}$  to  $\sim 800 \mu\text{J}$  and finally a REA6306 – 2P200 amplifying from  $\sim 800 \mu\text{J}$  to  $\sim 210 \text{ mJ}$ . The beam is configured to pass through each of these amplifiers in a double pass configuration while the beam size is magnified at each stage to match  $\sim 80\%$  of each amplifier's rod diameter. It is important to note that, in comparison to flashlamp pumped amplifiers, since these amplifiers are diode pumped, the absorption of the crystals is largely affected by the wavelength (and thus temperature) of the pumping diodes, which is being controlled by the temperature of the chillers cooling the system.

With this system we create beams of  $\sim 7$  mm in diameter and, depending on where we "sit" on the gain profile of the amplifiers' crystals, we have measured energies per pulse of up to 220 mJ per pulse. The pulse duration can be controlled by the arbitrary waveform generator controlling the IEOMs; with this system we can produce pulses with pulse durations ranging from  $\sim 10$  ns to  $\sim 1 \mu\text{s}$  at arbitrary temporal profiles and for pulses greater than 50 ns with no significant loss in output energy per pulse. Fig. 9 presents the heterodyned signal of the two pulses produced by the two arms of this system on a fast photodiode (Hamamatsu Photonics G6854 – 01) where the instantaneous frequency  $f(t)$  of the beat signal across the pulse duration has been analyzed using the method of Fee *et al.*<sup>17</sup>

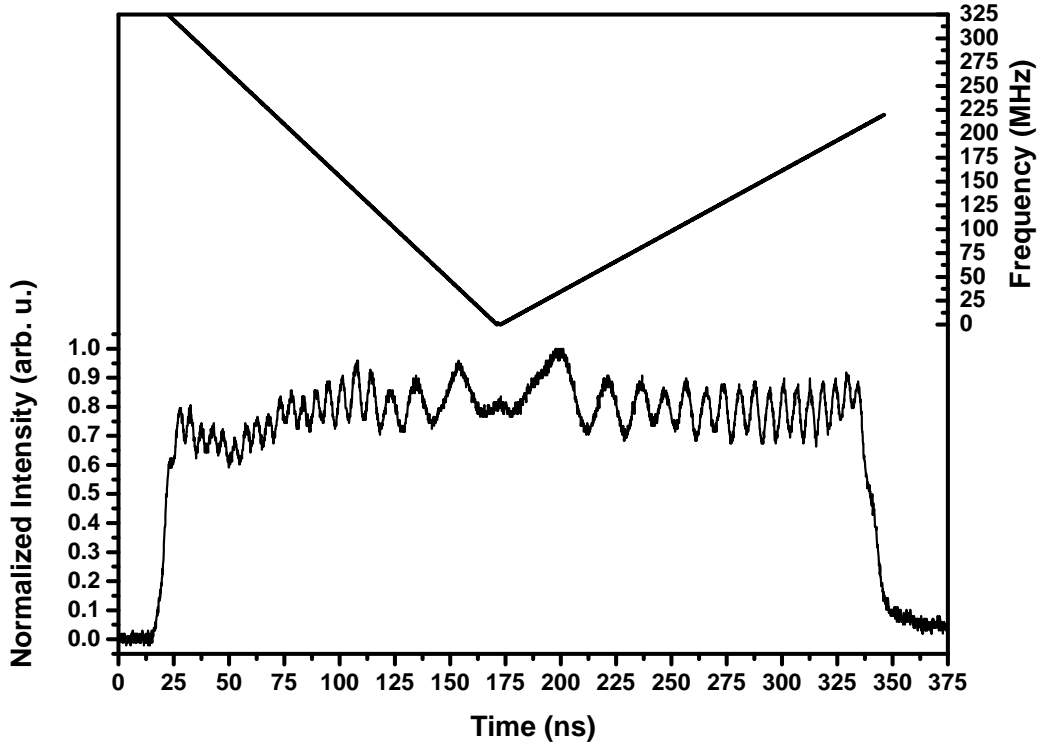


Figure 9. Heterodyned signal on a fast photodiode of the two pulses produced by this laser system (bottom). On the top of the graph is presented the instantaneous frequency  $f(t)$  of the beat signal across the pulse duration.

### 3. COHERENT RAYLEIGH-BRILLOUIN SCATTERING

With the laser system presented in the previous section we have got the ability to obtain a coherent Rayleigh-Brillouin spectrum employing the chirped lattice approach, in a single laser pulse. Fig. 10 presents how the beams produced from our laser system are laid out for a CRBS measurement. In fact, in Ref.<sup>9</sup> we have demonstrated this ability and we have used CRBS to determine the pressure and the polarizability of a gas or gas mixture of known composition. We have measured CRBS spectra and spectral integrals in a variety of gases and gas mixtures like air, CO<sub>2</sub>, SF<sub>6</sub> and He.

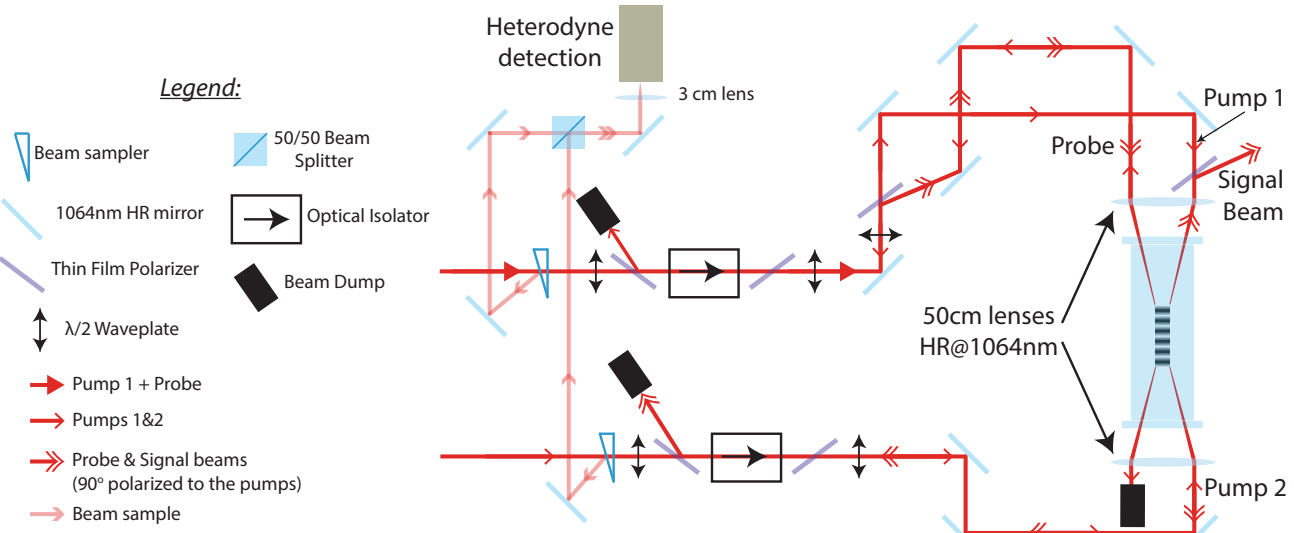


Figure 10. Beam layout for the single shot CRBS experiments. One of the beams is used as the pump while the second beam is split and used as the pump and probe. The probe's polarization is set to being normal to that of the pumps so that it does not interfere with them. The signal beam is counterpropagating one of the pumps and is being extracted with the use of a thin film polarizer.

We are currently working on employing CRBS for the measurement of nanoparticles in a graphitic arc discharge. The feasibility of the use of CRBS as such a tool was initially proposed in Ref.<sup>18</sup> where it was proposed that, instead of gas molecules as it has traditionally been the case for CRBS, the lattice sites now be populated with nanoparticles. Indeed, based on the fact that CRBS is a technique relying on the polarizability of the particles to be measured and, given the fact that the particles produced in a graphitic arc discharge (such as C<sub>60</sub> and carbon nanotubes) have got much higher polarizabilities than a gas molecule, a theoretical model to predict CRBS' sensitivity for nanoparticle measurement was developed.

For example, according to this model, for C<sub>60</sub> to be detected in an N<sub>2</sub> gas background a relation of  $N_{C_{60}}/N_{N_2} \geq 5 \times 10^{-6}$  must hold for the respective densities. With a polarizability of  $1.834 \times 10^{-40}$  C·m<sup>2</sup>·V<sup>-1</sup> and  $8.9 \times 10^{-39}$  C·m<sup>2</sup>·V<sup>-1</sup> for C<sub>60</sub> we can safely reach the estimate that if we can detect 10 Torr of air, we should have the ability to detect C<sub>60</sub> at a partial pressure of  $\sim 1$  mTorr. Of course, in this case we would not be launching phonons in nanoparticles, so the CRBS spectrum would just collapse to the Rayleigh peak from the width of which we would be able to derive the particle's temperature and mass. From the relative intensities of the CRBS signal across the various regions of the arc discharge, we should be able to derive the relative nanoparticle densities in the arc discharge while, if we calibrate the signal with a gas of known polarizability and density, we should be also be able to provide absolute nanoparticle densities. Fig. 11 shows a rendering of how the CRBS beams would be measuring in a graphitic arc discharge chamber.

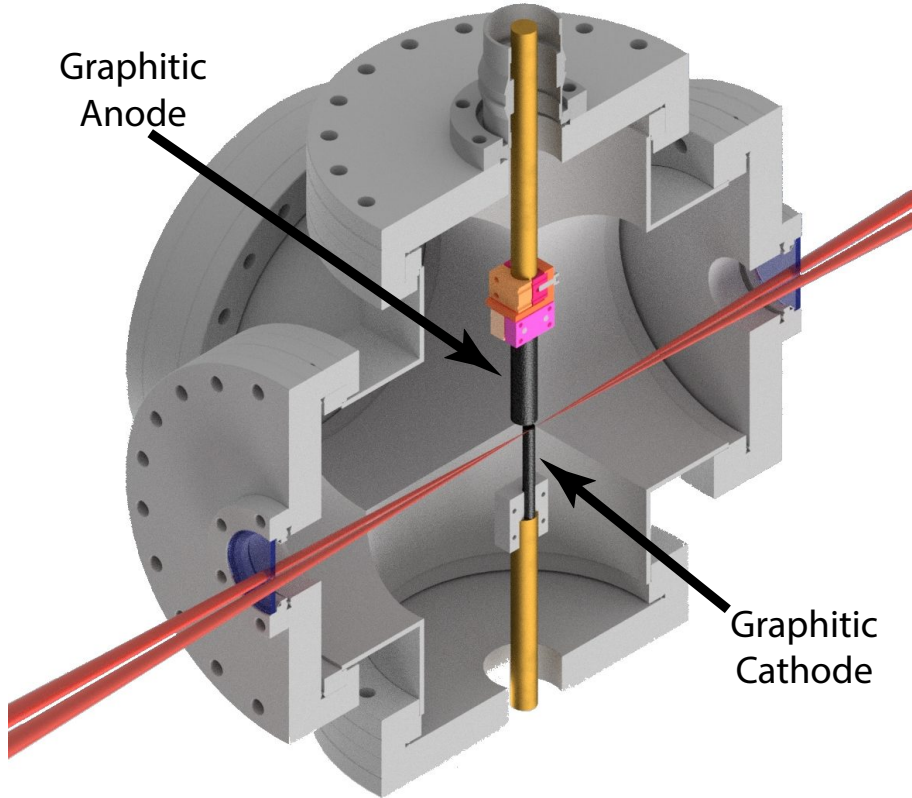


Figure 11. Rendering of the graphitic arc discharge used for the production of nanoparticles. Also shown are the CRBS beams crossing in the interelectrode gap and used for the detection of nanoparticles in the arc discharge.

## ACKNOWLEDGMENTS

The authors would like to acknowledge Prof. Peter Barker of University College London and Dr. Arthur Dogariu for useful discussions regarding the laser system. They would also like to acknowledge Mr. Yao-Wen Yeh and Mr. Alexandr Merzhevskiy for their assistance in setting up this experiment. The work is supported by the U.S. Department of Energy, Office of Science, Basic Energy Sciences, Materials Sciences and Engineering Division.

## REFERENCES

- [1] Grinstead, J. H. and Barker, P. F., "Coherent rayleigh scattering," *Phys. Rev. Lett.* **85**, 1222–1225 (Aug 2000).
- [2] Pan, X., Shneider, M. N., and Miles, R. B., "Coherent rayleigh-brillouin scattering," *Phys. Rev. Lett.* **89**, 183001 (Oct 2002).
- [3] Pan, X., Shneider, M. N., and Miles, R. B., "Coherent rayleigh-brillouin scattering in molecular gases," *Phys. Rev. A* **69**, 033814 (Mar 2004).
- [4] Graul, J. and Lilly, T., "Coherent rayleigh-brillouin scattering measurement of atmospheric atomic and molecular gas temperature," *Opt. Express* **22**, 20117–20129 (Aug 2014).
- [5] Cornell, B. M., Gimelshein, S. F., Shneider, M. N., Lilly, T. C., and Ketsdever, A. D., "Experimental and numerical analysis of narrowband coherent rayleigh–brillouin scattering in atomic and molecular species," *Opt. Express* **20**, 12975–12986 (Jun 2012).
- [6] Gerakis, A., Shneider, M. N., and Barker, P. F., "Coherent brillouin scattering," *Opt. Express* **19**, 24046–24054 (Nov 2011).

- [7] Vieitez, M. O., van Duijn, E. J., Ubachs, W., Witschas, B., Meijer, A., de Wijn, A. S., Dam, N. J., and van de Water, W., "Coherent and spontaneous rayleigh-brillouin scattering in atomic and molecular gases and gas mixtures," *Phys. Rev. A* **82**, 043836 (Oct 2010).
- [8] Meijer, A. S., de Wijn, A. S., Peters, M. F. E., Dam, N. J., and van de Water, W., "Coherent rayleighbrillouin scattering measurements of bulk viscosity of polar and nonpolar gases, and kinetic theory," *The Journal of Chemical Physics* **133**(16) (2010).
- [9] Gerakis, A., Shneider, M. N., and Stratton, B. C., "Remote-sensing gas measurements with coherent rayleigh-brillouin scattering," *Applied Physics Letters* **109**(3), 031112 (2016).
- [10] Lilly, T., Ketsdever, A., Cornell, B., Quiller, T., and Gimelshein, S., "Gas density perturbations induced by a pulsed optical lattice," *Applied Physics Letters* **99**(12) (2011).
- [11] Gerakis, A., Shneider, M. N., and Barker, P. F., "Single-shot coherent rayleigh&#x2013;brillouin scattering using a chirped optical lattice," *Opt. Lett.* **38**, 4449–4452 (Nov 2013).
- [12] Coppendale, N., Wang, L., Douglas, P., and Barker, P. F., "A high-energy, chirped laser system for optical stark deceleration," *Applied Physics B* **104**(3), 569 (2011).
- [13] Repasky, K. S., Switzer, G. W., and Carlsten, J. L., "Design and performance of a frequency chirped external cavity diode laser," *Review of Scientific Instruments* **73**(9), 3154–3159 (2002).
- [14] Siegman, A. E., [Lasers], University Science Books (1986).
- [15] Coppendale, N. P., "Manipulation of molecular motion using a high-energy chirped laser system," *Ph.D. Thesis, University College London* (2011).
- [16] Gerakis, A., "Controlling and probing molecular motion with optical lattices," *Ph.D. Thesis, University College London* (2014).
- [17] Fee, M. S., Danzmann, K., and Chu, S., "Optical heterodyne measurement of pulsed lasers: Toward high-precision pulsed spectroscopy," *Phys. Rev. A* **45**, 4911–4924 (Apr 1992).
- [18] Shneider, M. N. and Gimelshein, S. F., "Application of coherent rayleigh-brillouin scattering for in situ nanoparticle and large molecule detection," *Applied Physics Letters* **102**(17) (2013).